



Preservation of Natural Phase Balance in Multi-pass and Wire Arc Additive Manufacturing-Made Duplex Stainless Steel Structures

Farrokh Binesh, Alireza Bahrami, Mark Hebel, and Daryush K. Aidun

Submitted: 26 May 2020 / Revised: 27 January 2021 / Accepted: 13 February 2021 / Published online: 12 March 2021

This work investigates the effects of Ar-based shielding gases on the microstructure and phase balance of duplex stainless steel (DSS) depositions. The results are then used for fabrication of DSS walls using wire arc additive manufacturing (WAAM), and the microstructural characteristics and mechanical performance of the products are assessed. WAAM currently poses as one of the most interesting methods of manufacturing by enabling joining of materials to fabricate structures layer by layer. However, the extreme conditions imposed by the process, such as high heat inputs and re-melt and solidification of the deposited layers, could compromise the performance of the products. A detailed microstructural analysis is conducted on single layer and double layer depositions of DSS to assess the effects of different shielding gases on the ferrite/austenite phase balance in the specimens. The results show that the depositions shielded with a small fraction of carbon dioxide (CO₂) present better microstructural features in comparison to depositions shielded with the other selected gases. A mixture of 98%Ar + 2%CO₂ was employed for fabrication of a 60-layer DSS WAAM-made wall and some mechanical characteristics were studied. The mechanical examinations demonstrate that the properties of the parts fabricated using WAAM are comparable with their wrought counterparts.

Keywords additive manufacturing, duplex stainless steel, gas metal arc welding, inter-pass temperature, mechanical properties, microstructure

1. Introduction

Duplex ferritic-austenitic stainless steels (DSS) are of favorite structural materials in industries with hostile environments since the 1980s due to their desirable mechanical performance in such conditions (Ref 1). Their application has been evolving widely in chemical, oil, and gas, and marine industries, as a response to the demand for a combination of mechanical and corrosion resistance properties, and the high and volatile prices of alternative materials such as nickel-based alloys (Ref 2, 3). The name duplex originates from the natural balance of phases in the microstructure of this type of stainless steels, which approximately comprises equal proportions of austenite (γ) and delta-ferrite (δ) phases (Ref 4). Accordingly, DSSs take advantage of the properties of both ferritic and austenitic steels. It has been noted in the literature that in order to keep the desired mechanical and corrosion resistance properties of DSS alloys, a near equal amount of austenite and ferrite should be maintained (Ref 5, 6). Nevertheless, standard procedures such as gas metal arc (GMA) welding (especially in the case of multi-pass depositions) and novel

fabrication methods such as wire arc additive manufacturing (WAAM), significantly disturb this balance as well as the microstructural properties, such as the size and morphology of the grains (Ref 7-9). Therefore, it is a major concern for the industries that deal with DSSs to control the process and maintain the microstructural balance of ferrite and austenite phases in the fabricated parts.

The outstanding properties of DSS present them as an interesting material for additive manufacturing (AM) techniques such as WAAM. Gas metal arc-wire arc additive manufacturing (GMA-WAAM) is now a favorable alternative to conventional manufacturing methods for fabrication of monolithic components in industrial sectors such as automotive and oil and gas (Ref 10, 11). In WAAM, the material is deposited in layers at points where it is needed in accordance with the final geometry, for instance in a wall of welds (WoW) (Ref 12, 13). As a result of the layering process, the localized heat source will be reintroduced to points that have already been deposited. This process and its intrinsic associates adversely affect the balance of microstructure and cause a progressive decrease in the ferrite content in DSSs, which greatly influences the mechanical performance and corrosion properties of the produced part (Ref 14, 15). Eriksson et al. (Ref 16) studied the cold metal transfer of super duplex stainless steels (SDSS) using WAAM and maintained a ferrite content of 20–30%. Posch et al. (Ref 17) studied the effects of DSS cold metal transfer using WAAM and were able to achieve a ferrite content up to 35%. Hosseini et al. (Ref 18) investigated the evolution of microstructure in the last deposited layer of DSS using WAAM and reached a ferrite content of 40%, nevertheless, a small amount of sigma phase was observed in the phase boundaries. The precise value of 50/50 ferrite-austenite phases is difficult to achieve repeatedly, but a range of phase balances is acceptable for maintaining part quality from a mechanical

Farrokh Binesh, Mark Hebel, and Daryush K. Aidun, Mechanical and Aeronautical Engineering Department, Clarkson University, Potsdam, NY 13699; and Alireza Bahrami, Fulton Group North America, Pulaski, NY 13142. Contact e-mail: bineshf@clarkson.edu.

and metallurgical point of view (Ref 19). In this sense, extending the knowledge over the effects of significant process parameters such as the shielding gas and heat input seems inevitable in order to ensure the quality of performance in harsh circumstances in which these alloys are employed. Factors such as shielding gas, arc voltage and current, arc traveling speed (scanning speed), and the inter-pass temperature (IPT) are of significant parameters influencing the WAAM process conditions and the quality of the manufactured parts.

The shielding gas composition significantly influences the characteristics of the arc plasma, which has great effects on the heat transfer mechanism and mass transport in the weld pool (Ref 20). Pure argon (Ar) is the most common shielding gas in welding DSS (Ref 1, 21). Nevertheless, using pure Ar could lead to high austenite balance in the composition of the solidified material in case of multi-layer deposition (Ref 22); leading to deterioration of mechanical properties of the work-piece. The ferrite-austenite ratio also depends on the energy input of the employed GMA process (Ref 23). For DSSs, an approximate balanced microstructure in the weld zone (WZ) has been reported by adjusting the heat input between 0.5 and 2.5 kJ/mm (Ref 19). Since the duplex alloys initially solidify as ferrite, one might expect a higher fraction of ferrite in the final microstructure. However, in case the cooling rate is not high enough, austenite with various morphologies disperse in form of islands within the ferrite matrix (Ref 24, 25). Slow cooling rates could promote a higher ratio of austenite in comparison with ferrite, in company with deleterious precipitates, e.g., sigma (σ), Chi (χ), and nitrides such as Cr₂N (Ref 23, 26, 27). Controlling the inter-pass temperature (IPT) is one of the ways for stabilization of the temperature gradients and cooling rate to preserve the ferrite percentage, as well as avoiding unwanted precipitates (Ref 28, 29). In case of a duplex stainless steel, a range of 150–290 °C is suggested for applied IPT (Ref 30, 31).

In this study, wire arc additive manufacturing (WAAM) directed energy deposition (DED) is used to fabricate 2209 duplex stainless steel walls. Firstly, a detailed investigation on the microstructure evolution and phase balances of DSS2209 weld metals (WM) using several multi-components Ar-based shielding gases in company with controlled IPT is reported. Next, the results of these experiments were employed for manufacturing a 60-layer WAAM-made DSS wall, and the microstructural characteristics are investigated. Finally, the results for mechanical tension and 3-point bending tests on the DSS wall are presented and compared to wrought made specimens.

2. Experimental Set-up

2.1 Single Pass and Double Pass Depositions

Weldments were deposited using a Lincoln Electric GMA welding machine on 6.3 mm thick substrates in flat position designed as a butt joint (Ref 32). The DSS S32205 substrate plates were prepared mechanically by machining to dimensions of 150 mm long, 50 mm wide, and 6.3 mm thick, with 45° cuts at the edges, along the length of the substrates to produce V-grooves (Fig. 1). The consumable wire electrode used was DSS2209 commercially available as AWS ER2209 with 0.9 mm (0.035 in.) diameter. The chemical composition of

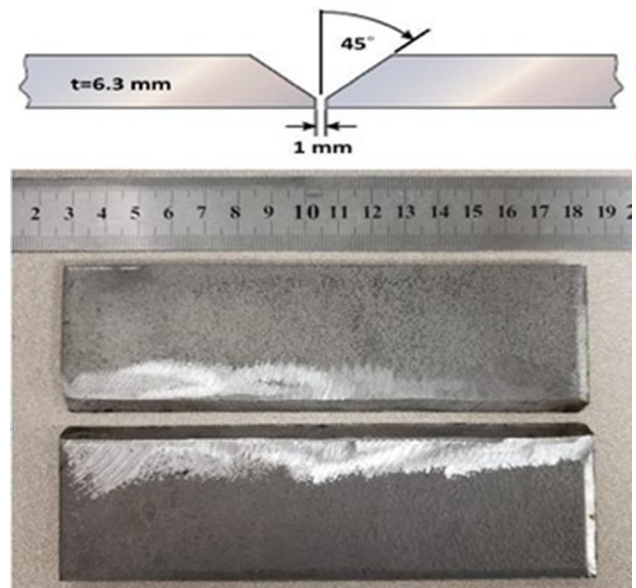


Fig. 1 DSS2205 substrates were cut in 45° angles to provide V-grooves

the DSS2205 substrate and the ER2209 wire is presented in Table 1.

All substrates were chemically cleaned with acetone to remove contaminants prior to initiation of deposition. Single pass and double pass depositions were fabricated using three different compositions of shielding gases (98%Ar + 2%CO₂, 92%Ar + 8%CO₂ and 63%Ar + 35%He + 2%CO₂) with a flow rate of 18 L/min to assess the balance of microstructure in each case. Figure 2 illustrates the weldments deposited with the employed Ar-based shielding gases and IPT of 250 °C. This measure is chosen considering the total time of manufacturing. Selecting an IPT near 200 °C could improve the microstructural characteristics of the product. Nevertheless, it would significantly add to the delay time in between layer depositions.

Properties of the constituent of the employed shielding gases are summarized in Table 2.

Since the heat source efficiency is an unknown parameter which greatly depends on the shielding gas composition as well as the arc length in this work, the maximum energy input represented by \dot{e}_m (kJ/mm) was calculated using Eq. 1,

$$\dot{e}_m = EI/V \quad (\text{Eq 1})$$

where E is the arc nominal voltage, I is the welding current, and V is the arc traveling speed. The welding parameters layout used in this work is listed in Table 3.

The cross-sections of the weld samples were polished from 240 to 1200 grit and then cloth-polished to 1 μm for a mirror-like finish. The products were etched for 4 seconds using an etchant solution with a composition of “100 ml HCl + 100 ml of ethanol + 5 g CuCl₂.” The revealed microstructures were examined by light optical microscopy (LOM) using a Nikon Eclipse L200 microscope and scanning electron microscopy (SEM) using a FESEM Joel 7400.

The ferrite content in the final microstructure was measured by a Fischer Feritscope MP3 using magnetic permeability of the WMs. The cross-section of single pass and double pass metallography samples extracted from the welds shielded with

Table 1 Chemical composition of the employed materials (wt.%)

Material	Ni	Cr	Nb	Mo	Ta	Al	C	Mn	Si	P	S	N	Cu	Fe
Substrate 2205	6.5	23	...	3.25	0.03	2.00	1.00	0.03	0.02	0.14	...	Balance
Wire ER2209	8.5	22.9	0.01	3.1	< 0.001	0.01	0.01	1.54	0.53	0.02	<0.01	0.16	0.05	Balance

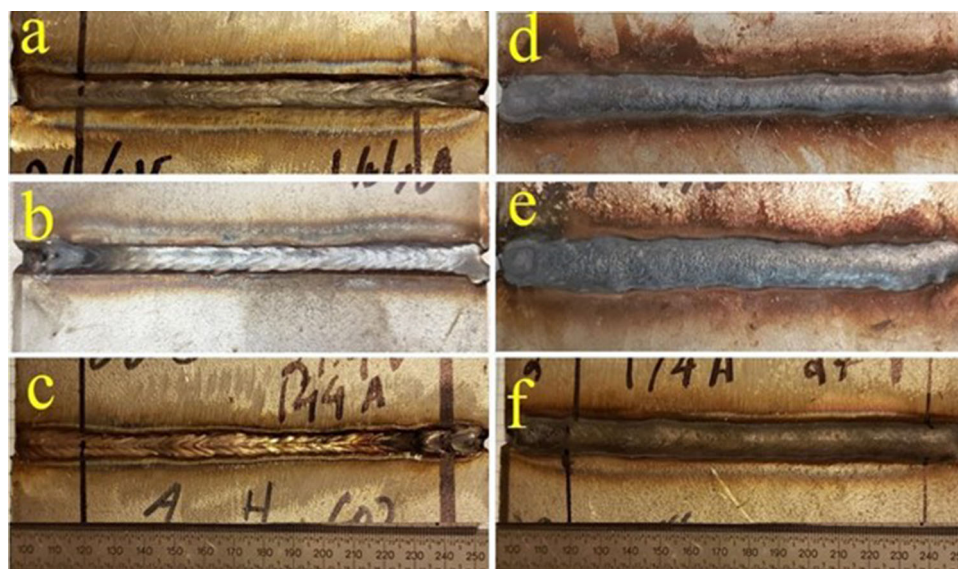


Fig. 2 Weldments with Ar-based shielding gases: (a) sample 1: single pass weld with 98%Ar + 2%CO₂, (b) sample 2: single pass weld with 92%Ar + 8%CO₂, (c) sample3: single pass weld with 63%Ar + 35%He + 2%CO₂, (d) Sample 4: double pass weld with 98%Ar + 2%CO₂ and 250 °C IPT, (e) sample 5: double pass weld with 92%Ar + 8% CO₂ and 250 °C IPT, (f) sample 6: double pass weld with 63%Ar + 35%He + 2%CO₂ and 250 °C IPT

Table 2 Properties of the constituents of the employed shielding gases for deposition of DSS2209

Properties	Ar	CO ₂	He
Density ($\frac{kg}{m^3}$)	1.78	1.98	0.18
Molecular weight ($\frac{g}{mol}$)	39.95	44.01	4
Ionization potential (eV)	15.7	14.4	24.5

98%Ar + 2%CO₂ is shown in Fig. 3, as an example to show the ferrite measurement approach. The horizontal measurements start in the base metal (BM) and are followed in one-millimeter increments within the HAZ and WZ toward the BM on the other side of the welds. The vertical ferrite measurements start at the center of the weld zone, from root through the top in one-millimeter increments.

2.2 WAAM Multi-layer Deposition

A semi-automatic mechanized GMA system as shown in Fig. 4 is used in this study for the WAAM process set-up. A mixture of 98%Ar + 2%CO₂ was employed as the shielding gas based on the microstructural results and phase balance analysis obtained from the multi-pass WM study in the first part of this work. The wall was built up to 60 layers with the AWS ER2209 (DSS2209) wire used in the multi-pass weld study and process parameters presented in Table 4, to the dimensions of 200 mm (8 in.) long, 125 mm (5 in.) high, 7 mm thick.

The material deposition took 34 ± 3 s for each layer. In order to maintain the 250 °C IPT, an infrared sensor was used to measure the temperature of the initial point of each pass. By the end of first layer, the temperature of the initial deposition point was 150 °C; so, there was no need for a delay and the second layer was deposited consecutively. For the second, third, and fourth layers, this measure was, respectively, 190, 210, 245 °C. Accordingly, there was no need to maintain the IPT for these particular layers as well. Passing the 5th layer, the time needed for reaching the IPT of 250 °C was always 150 ± 5 s up to the 60th layer, while the deposition time was still 34 ± 3 s for every layer.

2.3 WAAM Microstructural and Mechanical Characterization

The wall was sectioned, and the cross-section was studied under LOM and SEM following the standard polishing and etching processes described for the welds in the previous section. The ferrite content and microstructural phase balance were also studied from the base to top layers along the height of the wall.

Tension test and flexural bend test samples were separated from the wall for mechanical performance assessment and comparison to the wrought DSS test specimens (Fig. 5). The tension test samples were prepared according to ASTM E8/E8M standard, and the uniaxial tensile tests were performed using an Instron universal testing machine with a 100 kN tension load cell and a cross-head speed of 1.27 mm/min. In addition, the 3-point flexural bend tests were performed at the

Table 3 GMAW welding process parameters used for deposition of single pass and double pass DSS2209 welds

	Sample #	Arc voltage, V		Arc current, A		Energy input, KJ/mm
Single pass	Sample 1	21		144		0.60
	Sample 2	21		144		0.60
	Sample 3	21		144		0.60
Double pass		1st Pass	2nd Pass	1st Pass	2nd Pass	
	Sample 4	21	27	144	175	0.60-0.85
	Sample 5	18.5	26	145	180	0.60-0.85
	Sample 6	21	27	144	175	0.60-0.85

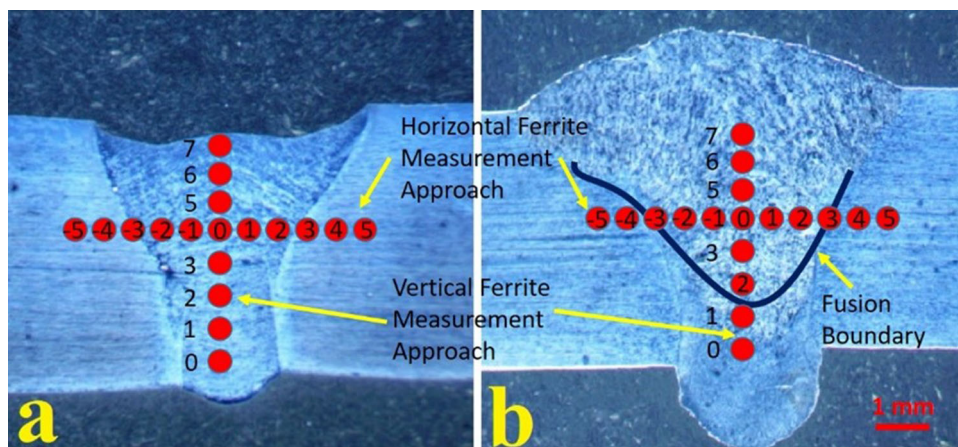


Fig. 3 The schematics of experimental ferrite measurement approach using the macrostructure images of: (a) the single pass deposition with 98%Ar + 2%CO₂ shield (b) the double pass deposition with 98%Ar + 2%CO₂



Fig. 4 Experimental set-up for building of 2209Ww

face of samples according to ASTM D790. The support span of the test fixture and width of the specimens were, respectively, 88.9 and 25.4 mm. The experiment was carried out at the face of the samples, with a 0.25 mm/min cross-head speed continued beyond the yield point of the specimens.

3. Results and Discussion

3.1 Weld Metals Ferrite Measurement and Microstructure

The macrographs of the selected weld sample cross-sections are presented in Fig. 6.

The weld samples which were fabricated using shielding gas containing 98%Ar + 2%CO₂ showed a deeper and narrower WZ with a higher fraction of ferrite phase and a more balanced microstructure. Ferrite contents were measured three times for each location as articulated in Sect. 2.1 and the mean results are illustrated in Fig. 7, 8, 9, and 10.

Figure 7 and 8, respectively, depicts the fraction of ferrite phase in the single pass welds in horizontal and vertical directions. Figure 7 demonstrates that the ferrite content

Table 4 Process parameters selected for fabrication of the wall deposited with 98%Ar + 2%CO₂ shielding gas mixture

WAAM parameters	Arc voltage, V	Arc current, A	Feeding rate, mm/s	IPT, °C	Scanning speed, mm/s
WoWIP250	18.5	140	142	250	5.8



Fig. 5 Removal of bend test samples (#1, #3, and #5), dimensions: 100 mm high, 12.5 mm wide, 2.5 mm thick; and tension test samples (#2, #4, and #6), dimensions: 100 mm high, 10 mm wide, 2.5 mm thick, $R = 6$ mm, gage length: 25 mm high, 6 mm wide; grip length: 30 mm high

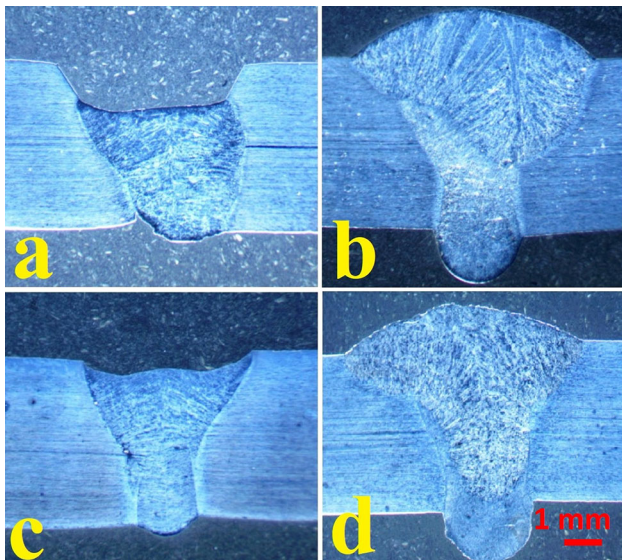


Fig. 6 Macrographs of cross-sections: (a) single pass with 63%Ar + 35%He + 2%CO₂, (b) double pass with 63%Ar + 35%He + 2% CO₂, (c) single pass with 98%Ar + 2%CO₂, (d) double pass with 98%Ar + 2%CO₂

decreases for all WMs as the location of measurement goes farther from the BMs toward the center of the weld. Nevertheless, the WMs deposited with 98%Ar + 2%CO₂ showed higher ferrite content compared to depositions with other shielding gases. Figure 8 depicts that there is an almost steady trend for the ferrite content of the single pass weldments deposited with 98%Ar + 2%CO₂ through the top surface of the welds, while this measure decreases for depositions with 92%Ar + 8%CO₂ and 63%Ar + 35%He + 2%CO₂. The minimum, maximum, and the average ferrite contents over all measured values in the single pass weld metals are listed in Table 5. The data points at the ends of the horizontal measurements are not considered since they are most affected by the BM dilution. According to Table 5, single pass depositions shielded by Ar mixed with 2% CO₂ presented the highest mean ferrite content with least dispersion.

Figure 9 and 10 illustrates the fraction of ferrite phase in the double pass weldments in horizontal and vertical

directions. The depositions shielded by 98%Ar + 2%CO₂ gas mixture showed higher ferrite phase balance compared to others. Based on these measurements, the welds carried out with the 63%Ar + 35%He + 2%CO₂ mixture showed the lowest ferrite contents both when measuring horizontally and vertically. It can be seen in Fig. 9 and 10 that with the increase in CO₂ fraction from 2 to 8%, the ferrite content noticeably drops, especially when measuring along the vertical centerline through the top (Fig. 10). Where the ferrite content is measured horizontally (Fig. 9), the welds deposited with 2% and 8% carbon dioxide contained almost equal amounts of ferrite in HAZs. However, the fraction of ferrite dropped as moving closer to the center of the WZ. The minimum, maximum, and the average ferrite contents over all measured values in the double pass WMs are listed in Table 6. The data points at the ends of the horizontal measurements are not considered since they are most affected by the BM dilution.

It can be seen in Tables 5 and 6 that regardless of the shielding gas employed, the mean fraction of ferrite decreases in double layer depositions compared to single layers even with implementation of the IPT. This can be attributed to the decrease in cooling rates when adding the second layers, while the heat added from deposition of the first layer has already reduced the temperature gradients. As it is listed in Table 6, the measure of ferrite in double layer depositions decreases by 9% when the fraction of CO₂ in the shielding gas is elevated from 2 to 8%. Also, the minimum and maximum ferrite phase percentage improved when using 2%CO₂ in the shielding gas composition. Later, it can also be seen in the microstructures depicted in Fig. 12 and 13 that using 2% CO₂ enhanced the phase balance and the morphology of the WMs to some extent.

The lower fraction of ferrite in depositions using shielding gases containing 8%CO₂ can be attributed to added heat input associated with higher fraction of CO₂ in the shielding gas among other causes such as different BM dilutions. Carbon dioxide is chemically reactive at high temperatures associated with GMAW process. As the temperature increases, CO₂ molecules can dissociate and release carbon monoxide (CO) and free oxygen atoms (O) within the arc plasma (Ref 33). Based on the added dissociation energy of CO₂, it is expected that the heat input in deposition with Ar + 2%CO₂ and Ar + 8%CO₂ shielding gases to be higher compared to pure Ar

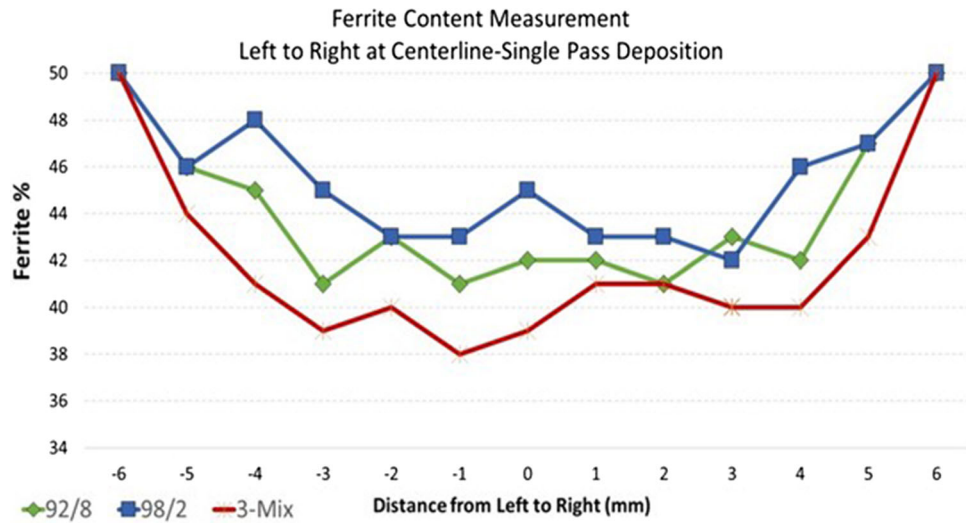


Fig. 7 Ferrite content measured from left to right at the horizontal centerline-single pass depositions

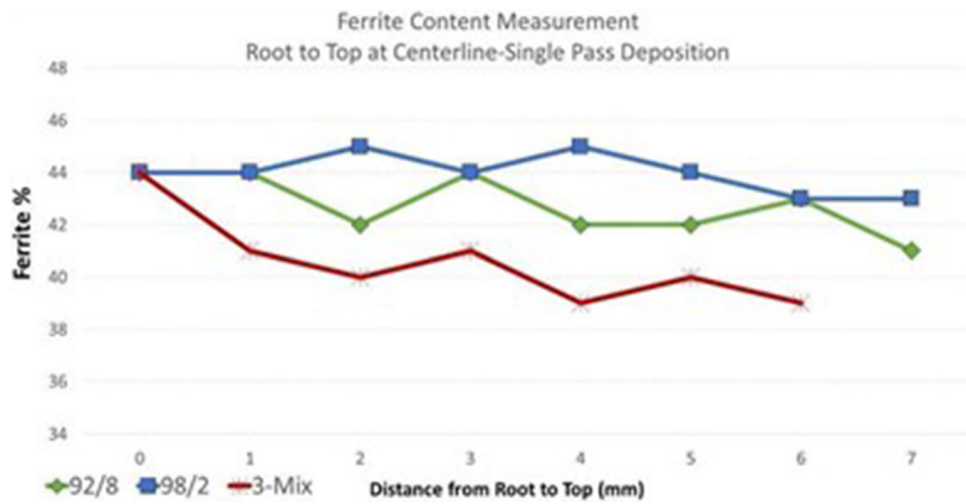


Fig. 8 Ferrite content measured from root to top at the vertical centerline-single pass depositions

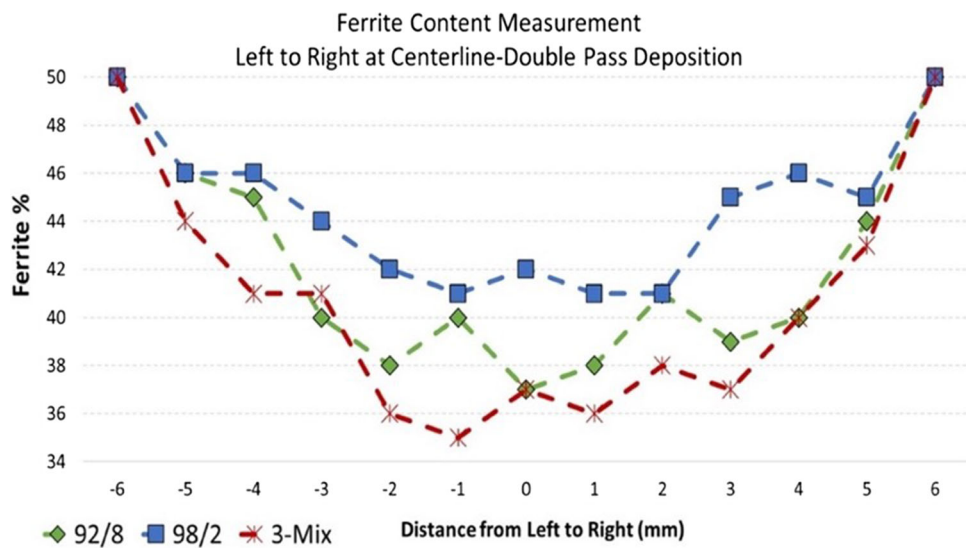


Fig. 9 Ferrite content measured from left to right at the horizontal centerline-double pass deposition

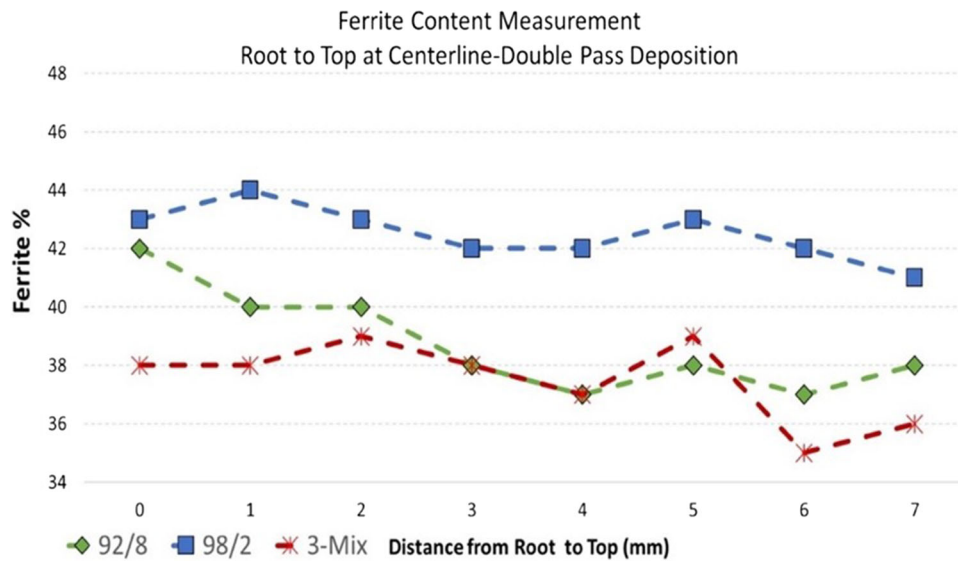


Fig. 10 Ferrite content measured from root to the top at vertical centerline-double pass depositions

Table 5 Ferrite content statistical data summary for single pass weld metal depositions

Shielding gas composition	Minimum	Maximum	Mean	SD
92%Ar + 8%CO ₂	41	45	42.8	1.72
98%Ar + 2%CO ₂	42	48	44.4	1.45
63%Ar + 35%He + 2%CO ₂	38	41	40.1	1.68

Table 6 Ferrite content statistical data summary for the double pass weld metal depositions with 250 °C IPT

Shielding gas composition	Minimum	Maximum	Mean	SD
92%Ar + 8%CO ₂	37	45	39.0	2.70
98%Ar + 2%CO ₂	41	46	43.1	1.78
63%Ar + 35%He + 2%CO ₂	35	41	38.2	2.53

(Ref 34, 35). The heat input would be higher when the fraction of CO₂ is elevated (8% in comparison with 2%).

The WM protected with Ar + He + CO₂ presented lower ferrite contents in comparison with WMs deposited with Ar + CO₂ compositions in this study. According to Table 6, they also showed the lowest minimum and maximum ferrite content compared to other samples. Considering the weld pool protected by Ar + 35%He + 2%CO₂, the ionization energy of He is much greater than that of Ar and dissociation energy of CO₂ (Table 2). The higher ionization energy of He means that higher arc voltage is required to trigger and maintain the arc plasma. As a result, the voltage drop in the electric arc would be higher by addition of He to pure Ar, and higher power would be conveyed to the work-piece. Therefore, it can be concluded that in the case of WMs shielded by Ar + 35%He + 2%CO₂, more heat input is transferred to melt pool, in comparison to WMs using Ar + 2%CO₂ and Ar + 8%CO₂. Figure 6 illustrates a large and parabolic fusion area for WM deposited with Ar + 35%He + 2%CO₂ and a narrow and deep penetration for WM deposited with Ar + 2%CO₂.

The DSS2205 base metal (BM) containing almost equal δ -ferrite (BCC) and γ -austenite (FCC) content is shown in Fig. 11. As it can be seen in Fig. 11(a) and (b), the texture of DSS microstructure is different in the rolling direction compared to other dimensions. The light color represents the ferrite phase as the continuous matrix, and the dark color represents the austenite phase, elongated in rolling direction as islands within the ferrite matrix.

The microstructures of the weld metals are presented in Fig. 12 and 13. Figure 12 illustrates the microstructure of single pass welds shielded using the three different gases and Fig. 13 shows the microstructure of double pass welds deposited with the same shielding gases, in company with the IPT.

The presented microstructure in Fig. 12 and 13 is taken at the center of the weld metals using a uniform magnification. The morphology and arrangement of the austenite phase within the ferrite matrix vary depending on the shielding gas composition and the implemented IPT. As shown in Fig. 12(a), the WMs deposited with 98%Ar + 2%CO₂ show a more balanced microstructure considering the composition of ferrite and austenite phases as well as the morphology of the austenite grains. Austenitic-ferritic DSSs solidify as ferrite phase and stay fully ferritic until temperature falls below ferrite solvus temperature. When the temperature drops below this threshold, austenite initially emerges at the ferrite grain boundaries. The austenite phase also emerges as typical forms of grain boundary austenite (GBA), Widmanstätten austenite (WA), and intragranular austenite (IGA) within the ferrite grain boundaries. As depicted in Fig. 12(c), the fraction of austenite is noticeably higher in depositions made with 63%Ar + 35%He + 2%CO₂, which is in correlation with ferrite content measurements given in Fig. 7 and 8. It can be deduced from Fig. 13(a), (b) and (c) that the weld metals with 98%Ar + 2%CO₂ show better microstructure, with a more symmetric balance of austenite and less dispersion in the austenite phase configuration, in addition to higher ferrite content compared to the rest of the depositions (Fig. 9 and 10). A well-adjusted 1:1 phase balance in DSSs can constrain the precipitation of harmful phases (such as sigma phase) and deliver better mechanical properties for the manufactured structure. Accord-

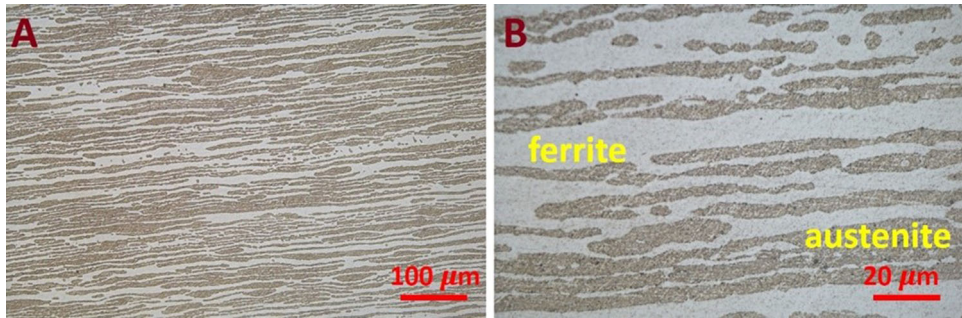


Fig. 11 DSS2205 BM microstructure containing almost equal amounts of δ -ferrite and γ -austenite (A) low magnification (B) high magnification

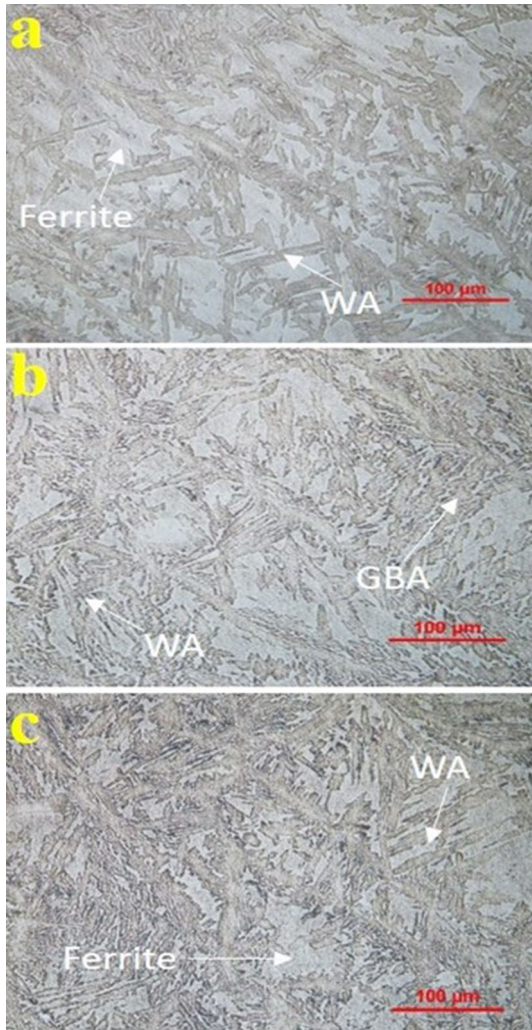


Fig. 12 Austenite morphologies (dark color) within ferrite matrix (light color). Grain boundary and Widmanstätten Austenites are marked in: (a) single pass weld metal shielded with 98%Ar + 2%CO₂, (b) single pass weld metal shielded with 92%Ar + 8%CO₂, (c) single pass weld metal shielded with 63%Ar + 35%He + 2%CO₂

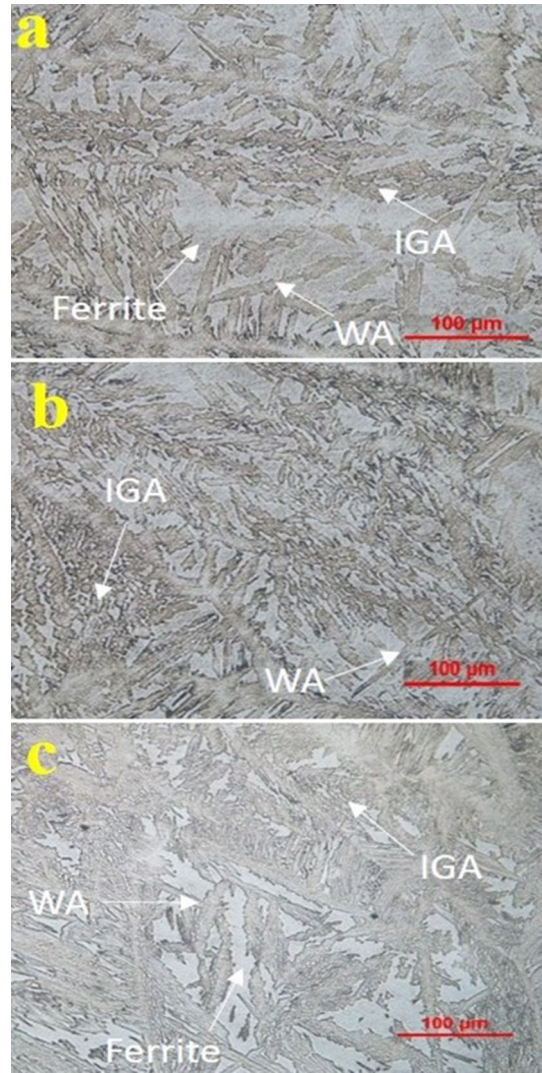


Fig. 13 Austenite morphologies (dark color) within ferrite matrix (light color). Grain boundary, Widmanstätten, and intragranular austenites are marked in: (a) double pass weld metal shielded with 98%Ar + 2%CO₂, 250 °C IPT (b) double pass weld metal shielded with 92%Ar + 8%CO₂, 250 °C IPT (c) double pass weld metal shielded with 63%Ar + 35%He + 2%CO₂, 250 °C IPT. The sample (a), associated with 98%Ar + 2%CO₂, 250 °C IPT shows higher fraction of ferrite phase in comparison to others.

ing to Lippold and Kotecki (Ref 1), the WMs should meet a minimum content of 30%, for ferrite and austenite, to avoid the presence of harmful phases. As shown in Fig. 13(c), the fraction of austenite with larger grain size is noticeably higher in the deposition using 63%Ar + 35%He + 2%CO₂, even with employment of the controlled IPT.

3.2 WAAM-Made Wall Ferrite Measurements and Microstructure

Based on the results obtained in Sect. 3.1, the 98%Ar + 2%CO₂ shield gas is employed for manufacturing a 60-layer wall in company with a controlled IPT. The ferrite content in the microstructure of the wall was measured using the magnetic permeability of the ferrite phase (Fig. 14). The initial layers contain higher fraction of δ -ferrite (41-46%) and finer WA in comparison to the middle layers (37-40%), as a result of the higher cooling rate provided by the substrate BM. The fraction of ferrite stands almost steady after the fourth layer through the top near 39%, which is significantly higher (10%) compared to the walls made with pure Ar as the shielding gas, particularly in higher layers near the top of the wall (Ref 22).

Figure 15 shows the microstructure of different sites along the height of the wall, such as the base metal (BM), heat-affected zone (HAZ), and the WAAM layers. The fraction of ferrite and austenite is almost equal in the BM. It can be seen that the grains show a rolling microstructure (white arrow shows the rolling direction) in the BM. Passing the fusion boundary (FB), the austenite phase (darker color) has grown in high temperature within ferrite matrix with typical morphologies: grain boundary austenite (GBA), intragranular (IGA), and Widmanstätten (WA); with a diffusion-based mechanism during the solidification process. The austenite grains are elongated in the thermal diffusion direction (Ref 36). The higher cooling rate involved in layers close to the FB, in company with reheating process in these layers causes a higher fraction of ferrite in the initial layers.

Since the rising thermal cycle leads to solid-state grain growth, it is likely to have larger grain sizes at higher layers of

the wall (Ref 37, 38). The decreasing temperature gradient along the height of the wall accelerates the growth of grain size as the later layers are deposited (Ref 22, 39). Furthermore, due to the larger molten pool and slower cooling in walls made with the wire-fed AM systems, it is expected to have a coarser microstructure compared to parts made with other techniques such as the powder-based AM. However, it seems that the employment of IPT in this work has ameliorated the grain coarsening effect as it is observed in Fig. 15. By engaging the IPT in the process, we help restoring the temperature gradient as farther the deposited layer gets from the BM. The size of austenite grains evidently remained in the same order (mostly under 100 Microns) in the middle layers through the top of the wall (Fig. 15, 16, 17).

When a layer of deposition is completed, a certain amount of heat dissipates through the molten pool, the body of the wall, and the substrate, which will be gradually transferred via conduction and convection. The arc power and the heat input transferred to the work-piece can be controlled by using appropriate process parameters, such as the welding voltage and current. In multi-pass welding and multi-layer WAAM deposition, the addition of subsequent layers, further decreases the temperature gradient, which itself reduces the cooling rate and eventually the ferrite content (Ref 1).

Based on the chemical composition of DSS2209, δ -ferrite as the first precipitating phase starts to transform to austenite at its solvus temperature. As the cooling continues in the temperature interval (1200-900 °C) under the δ -ferrite solvus temperature, the austenite phase begins to emerge at ferrite grain boundaries (GBA). Next, Widmanstätten austenite (WA) and intragranular austenite (IGA) grow as islands within the ferrite matrix. Nevertheless, an appropriate cooling rate (higher than 50 °C/s) in the indicated temperature range could slow down the precipitation of austenite phase as described by Verma, and Taiwade (Ref 30), and lead toward a more balanced microstructure. Furthermore, reheating the underlying layers with a slow cooling rate within the temperature range of 900–1050 °C accelerates the diffusional transformation of ferrite phase to austenite (Ref 40). In this sense, the high temperature gradient

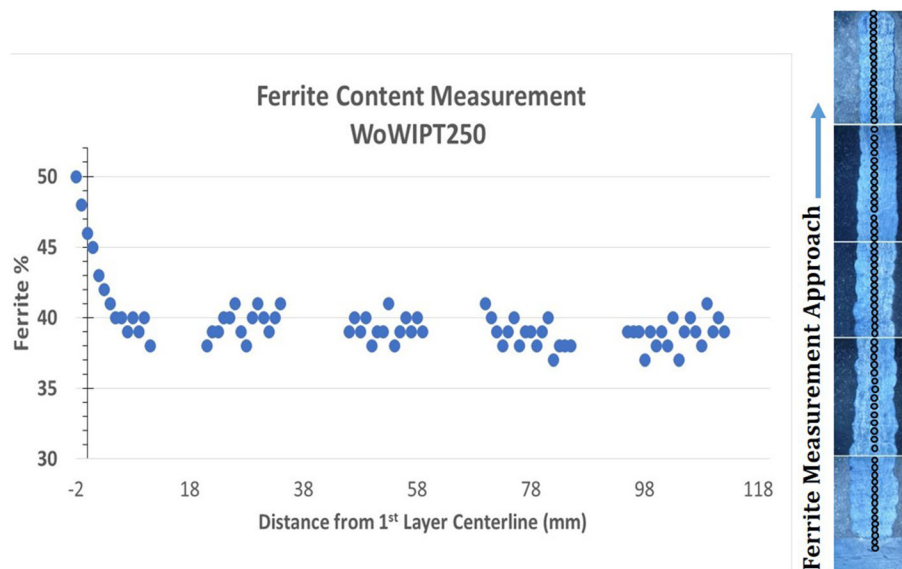


Fig. 14 Ferrite content measurement for WoWIP250; the right-hand macrographs illustrate the cross-section of the wall through the top along with the ferrite measurement locations

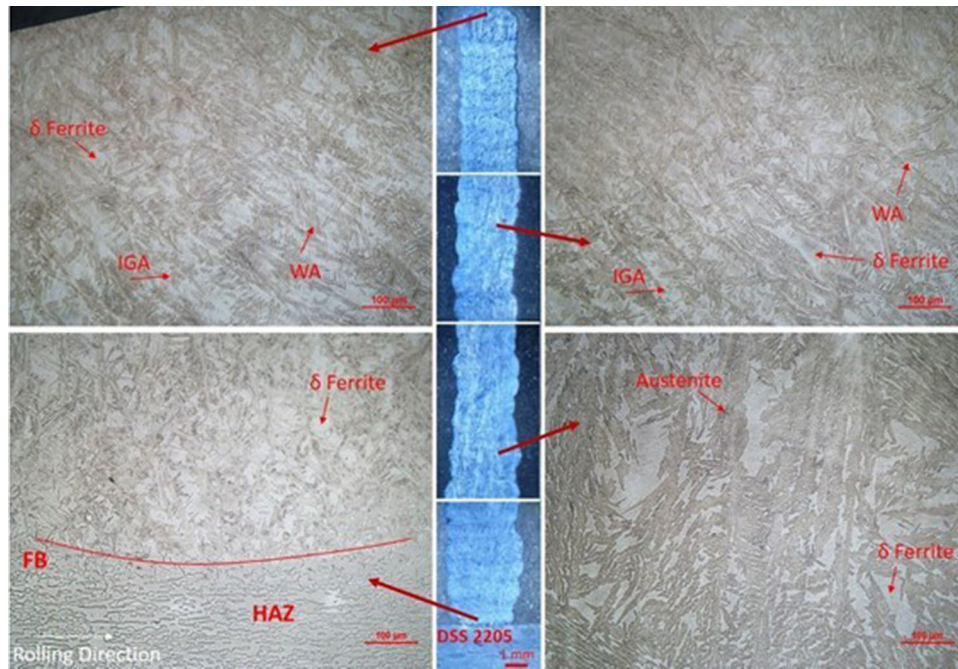


Fig. 15 Microstructure of the wall fabricated with mixture of 98%Ar + 2%CO₂ as shielding gas and 250 °C IPT. The lighter color represents the ferrite matrix in which different austenite morphologies can be seen in darker shades. Grain boundary, Widmanstätten, and intragranular austenites are marked along the height of the wall.

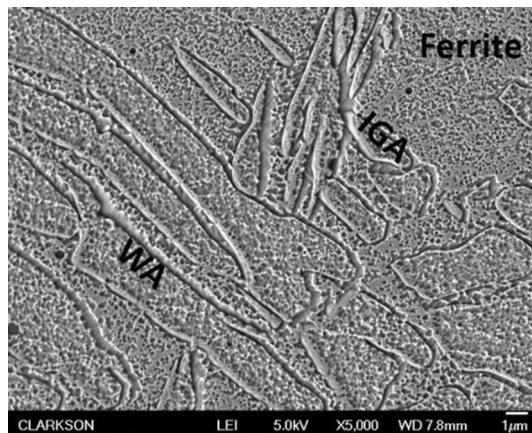


Fig. 16 WAAM 2209 microstructure (10th layer). Widm

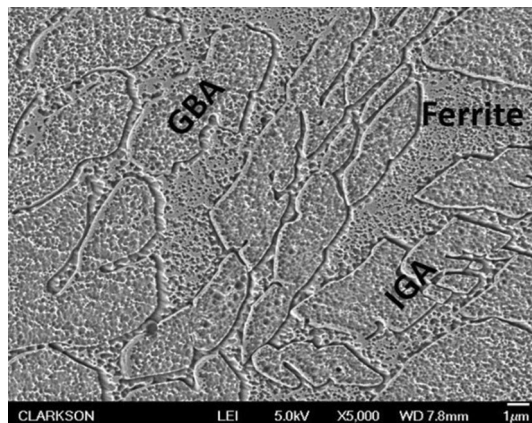


Fig. 17 WAAM 2209 microstructure (50th layer)

in the initial layers (provided by the substrate) leads to a lower fraction of austenite in the microstructure (Fig. 15). As the layers go higher without adopting an IPT, the reduction of temperature gradients decreases the cooling rate that leads to higher fraction of austenite and an unbalanced microstructure (Ref 22). The implementation of IPT restores the temperature gradients induced by multi-layer depositions. This provides a higher and steadier cooling rate, which can result in a higher ferrite content in the phase balance comparing to depositions without IPT.

Figure 16 and 17 demonstrates the SEM micrographs of the wall's body at 10th and 50th layer. No intermetallic phases such as sigma, or other defects (cracks) were observed through the top layers. (The small dark dots in the micrographs are produced by the polishing process.) Further, the size of the grains remains in the same order from 10th layer up to the 50th layer, which accents the importance of using the IPT.

3.3 Mechanical Characterization

The phase balance and microstructural characteristic of the multi-pass welds and the multi-layered wall deposited with the selected shielding gas were deliberated in the previous sections. The mechanical performance of the samples extracted from the DSS2209 wall is measured by the flexural bend tests and unidirectional tension tests, and the results are presented in the current section. The mechanical performance of DSSs is influenced by their phase balance and microstructure, and the microstructure itself is under the influence of the chemical composition and the cooling rate (Ref 41).

3.3.1 Flexural Bend Test. The mechanical performance of the WAAM samples was assessed in comparison to their wrought counterparts by a flexural 3-point bend study, carried out for three WAAM (Samples 1, 3, and 5 as shown in Fig. 5)

and one wrought beam specimens. A WAAM sample after the test is presented in Fig. 18 and the resulting flexural stress–strain curves are presented in Fig. 19. The drops and the plateau at the final stage of the tests for all three of the WAAM samples could be due to delamination, nonetheless, no sign of cracks or other defects were visible on the surface of the specimens.

The key characteristics of the flexural stress–strain curves are presented in Table 7. The same ductile behavior occurred in all WAAM made and wrought specimens; nevertheless, the average flexural strength of the WAAM samples was 4% higher than the wrought one. The average yield stress and flexural

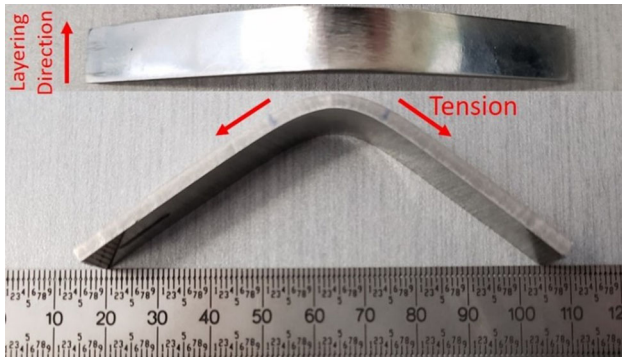


Fig. 18 Bend test WAAM sample (WoWIP250B03) after the test

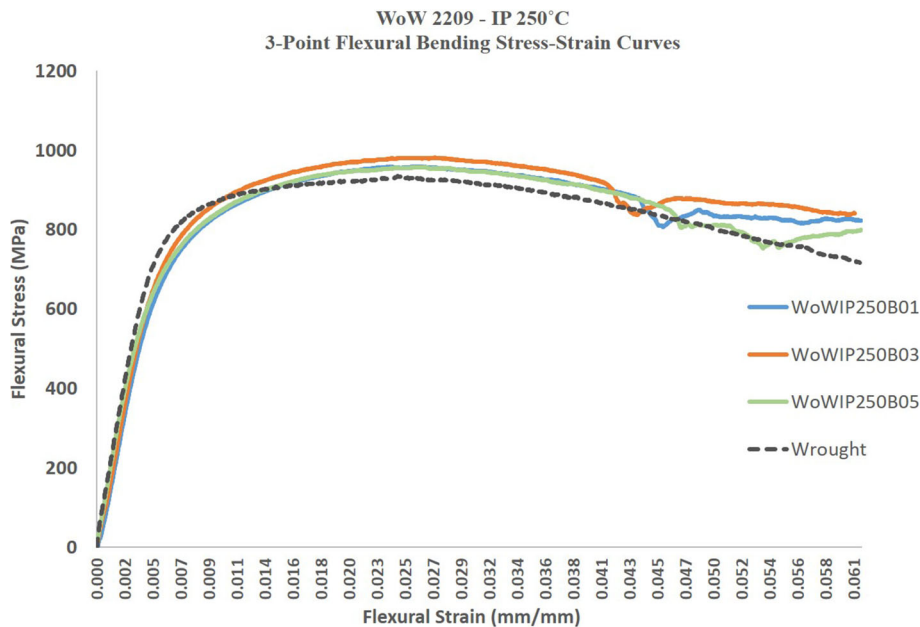


Fig. 19 Flexural 3-point bend test results for WAAM specimens and wrought specimen

Table 7 Flexural 3-Point bend test results for the DSS2209 WAAM specimens compared to the DSS2205 Wrought

Specimen	Flexural bending strength, MPa	Yield stress, MPa	Flexural Young modulus, GPa	Fracture stress, MPa
WoWIP250B01	948	766	163	823
WoWIP250B03	970	779	169	841
WoWIP250B05	957	770	171	799
Wrought 2205	924	788	180	718

modulus of the WAAM samples were only 3% and 7%, respectively, lower than the wrought sample.

3.3.2 Unidirectional Tension Test. The tensile test study was carried out for three samples extracted from the wall in the build direction. All samples showed ductile mode of fracture and the mechanical characteristics such as strength and ductility demonstrated very good uniformity from left to right of the wall. Figure 20 illustrates the WAAM-made and wrought samples after the tension tests.

The stress–strain curves for these samples are presented in Fig. 21 and the results are listed in Table 8, in company with the tensile test properties for a wall made with pure Ar as shielding gas and standard ER2209 (DSS2209) Wire. The average ultimate tensile strength (UTS) of the samples extracted from the wall is only 6% lower than wrought 2205 and 1% higher than ER2209. The average yield stress was, respectively, 10% and 5% lower than the wrought 2205 and ER2209. The samples extracted from the wall also showed better performance compared to the WAAM sample deposited with pure Ar without IPT (UTS = 682 MPa, YS = 480 MPa).

The fractured surface of the middle WAAM sample (WoWIP250T04) was examined by SEM following the test as shown in Fig. 22. The samples demonstrated ductile fracture behavior with dimples along the same direction. The fractured surfaces consisted of many dimples which indicates ductile fracture under unidirectional load; however, the geometry and size of the dimples were different in the WAAM sample compared to the wrought (Ref 22).

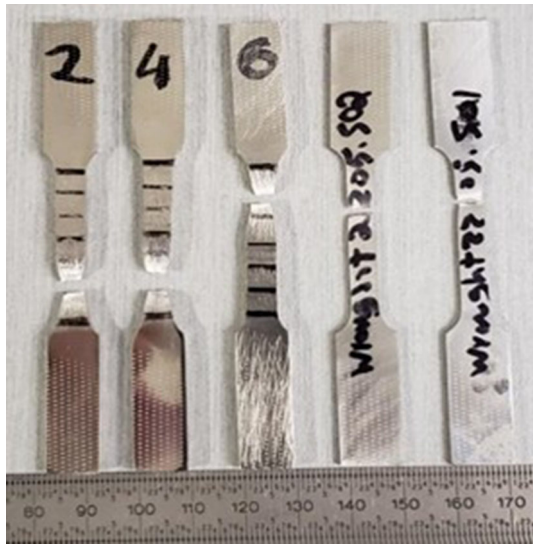


Fig. 20 WAAM-made DSS2209 and wrought tension test coupons after the test

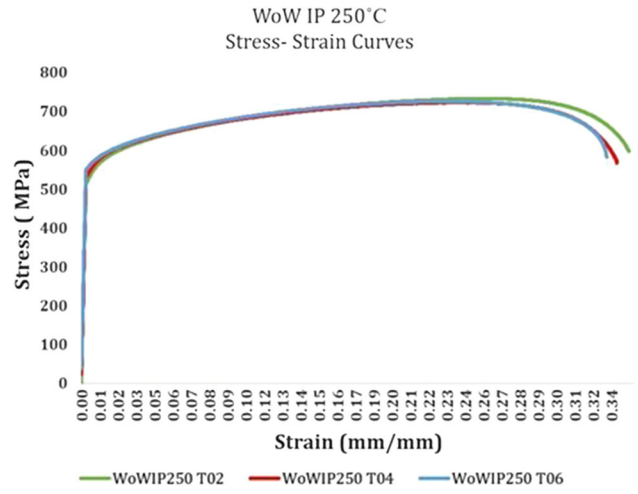


Fig. 21 Tension test stress–strain curves for samples extracted from WAAM-made wall

Table 8 Comparison of the tension test results for WAAM deposited DSS2209 and wrought metal

Specimen	UTS, MPa	YS, MPa	Fracture stress, MPa	Fracture strain
WoWIP250T02	733	521	598	0.35
WoWIP250T04	723	533	562	0.33
WoWIP250T06	726	549	579	0.33
Wrought 2205	779	590	491	0.34
WoW (Pure Ar) (Ref 22)	682	480
Data Sheet (Ref 42)	720	560

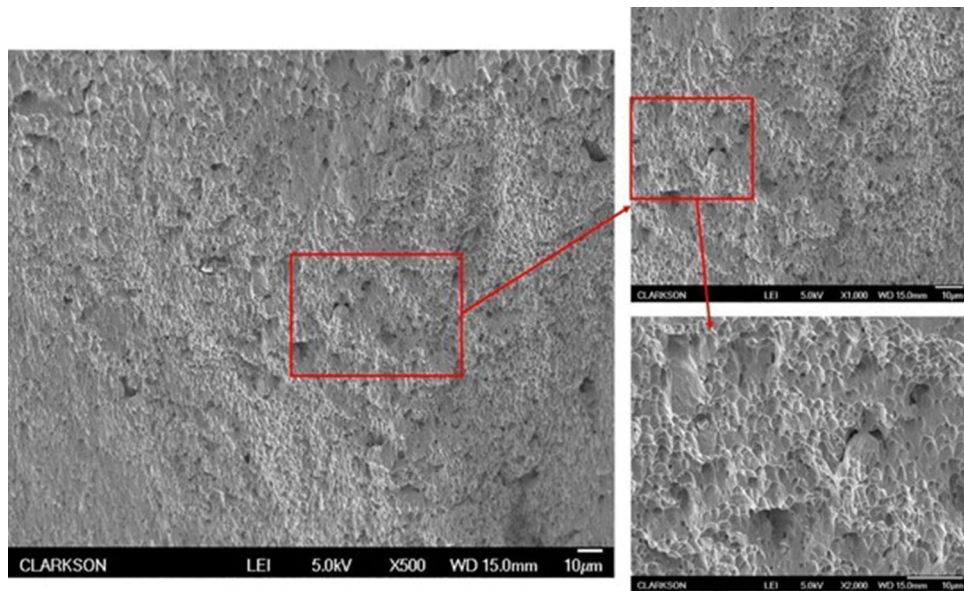


Fig. 22 WAAM 2209 tension test fractured surface—magnifications: 500 ×-1000 ×-2000 ×

4. Conclusion

This investigation assessed the effects of Ar-based shielding gases in company with IPT in deposition of multi-pass and multi-layer DSS2209. Based on our observations, the composition of shielding gases influenced the fraction of ferrite and microstructure in DSS2209 depositions. The following conclusions can be extracted from the current study:

- The intense thermal cycles inflicted on DSS2209 during the WAAM process had a deteriorating impact on the phase balance in microstructure and the ferrite content dropped compared to wrought counterparts (50% ferrite / 50% austenite), even with the implementation of IPT. No lack of fusion was observed based on the metallographic investigations.
- The WMs deposited using Ar mixed with 2% CO₂ presented the best microstructural characteristics and phase balance among the selected shielding gases. Therefore, this shielding gas was selected to be used in fabrication of a 60-layer WAAM-made wall. The microstructural analysis of the wall showed that it benefits from a relatively balanced microstructure compared to walls fabricated with pure Ar. No intermetallic phases such as sigma, or other defects were observed in the welds or WAAM multi-layer depositions through the top layers.
- The results of the tension tests and the flexural bend tests showed that the mechanical properties of the WAAM-made wall are comparable to its wrought counterparts. The average UTS of WAAM-made DSS2209 samples was measured just 6% below the wrought DSS2205. Nevertheless, this measure was still 6% higher than the UTS for samples fabricated with pure Ar, while the ferrite content was improved by 10%. The average flexural strength of the WAAM-made samples in the build direction was 4% higher compared to the wrought counterparts.

References

1. J.C. Lippold and D.J. Kotecki, *Welding Metallurgy and Weldability of Stainless Steels*, Wiley, 2005
2. S.J. Morrow, Materials Selection for Seawater Pumps, *Proceedings of the 26th International Pump Users Symposium*, 2010, Turbomachinery Laboratory, Texas A&M University
3. G. Krolczyk, P. Nieslony, S. Legutko and I. Samardzic, Investigation of the Physical Parameters of Duplex Stainless Steel (DSS) Surface Integrity After Turning, *Metalurgija*, 2015, **54**(1), p 87–90
4. V.A. Hosseini, M. Thuvander, S. Wessman and L. Karlsson, Spinodal Decomposition in Functionally Graded Super Duplex Stainless Steel and Weld Metal, *Metall. Mater. Trans. A*, 2018, **49**(7), p 2803–2816
5. B. Messer, V. Opera, and A. Wright, Duplex Stainless Steel Welding: Best Practices, *Stainless Steel World*, 2007
6. T.F.A. Santos, R.R. Marinho, M.T.P. Paes and A.J. Ramirez, Microstructure Evaluation of UNS S32205 Duplex Stainless Steel Friction Stir Welds, *REM Rev. Esc. Minas*, 2013, **66**(2), p 187–191
7. S. Kou, *Welding Metallurgy*, Wiley, 2003
8. B. Varbai and K. Majlinger, Thermoelectric Power Measurements on Duplex Stainless Steel Weldments, May 23–25, 2018, (Miskolc), *2nd International Conference on Vehicle and Automotive Engineering*, p 789–99
9. M.A. García-Rentería, V.H. López-Morelos, R. García-Hernández, L. Dzib-Pérez, E.M. García-Ochoa and J. González-Sánchez, Improvement of Localised Corrosion Resistance of AISI 2205 Duplex Stainless

Steel Joints Made by Gas Metal Arc Welding Under Electromagnetic Interaction of Low Intensity, *Appl. Surf. Sci.*, 2014, **321**, p 252–260. <https://doi.org/10.1016/j.apsusc.2014.10.024>

10. H. Geng, J. Li, J. Xiong, X. Lin and F. Zhang, Geometric Limitation and Tensile properties of Wire and Arc Additive Manufacturing 5A06 Aluminum Alloy Parts, *J. Mater. Eng. Perform.*, 2017, **26**(2), p 621–629
11. M. Abbaszadeh, J.R. Hönnige, F. Martina, L. Neto, N. Kashaev, P. Colegrove, S. Williams and B. Klusemann, Numerical Investigation of the Effect of Rolling on the Localized Stress and Strain Induction for Wire + Arc Additive Manufactured Structures, *J. Mater. Eng. Perform.*, 2019, **28**(8), p 4931–4942
12. V. Manvatkar, A. De and T. Debroy, Spatial Variation of Melt Pool Geometry, Peak Temperature and Solidification Parameters During Laser Assisted Additive Manufacturing Process, *Mater. Sci. Technol.*, 2015, **31**(8), p 924–930
13. W.E. Frazier, Metal Additive Manufacturing: A Review, *J. Mater. Eng. Perform.*, 2014, **23**(6), p 1917–1928
14. W.J. Sames, F.A. List, S. Pannala, R.R. Dehoff and S.S. Babu, The Metallurgy and Processing Science of Metal Additive Manufacturing, *Int. Mater. Rev.*, 2016, **61**(5), p 315–360
15. M.A. Makhdoom, A. Ahmad, M. Kamran, K. Abid and W. Haider, Microstructural and Electrochemical Behavior of 2205 Duplex Stainless Steel Weldments, *Surfac. Interfaces*, 2017, **9**, p 189–195
16. M. Eriksson, M. Lervåg, C. Sørensen, A. Robertstad, B.M. Brønstad, B. Nyhus, R. Aune, X. Ren, and O.M. Akselsen, Additive Manufacture of Superduplex Stainless Steel Using WAAM, *MATEC Web Conference*, EDP Sciences, 2018, p 188
17. G. Posch, K. Chladil and H. Chladil, Material Properties of CMT—Metal Additive Manufactured Duplex Stainless Steel Blade-Like Geometries, *Weld World*, 2017, **61**(5), p 873–882
18. V.A. Hosseini, M. Högström, K. Hurtig, M.A.V. Bermejo, L.E. Stridh and L. Karlsson, Wire-Arc Additive Manufacturing of a Duplex Stainless Steel: Thermal Cycle Analysis and Microstructure Characterization, *Weld World*, 2019, **63**(4), p 975–987
19. A. Vinoth Jebaraj, L. Ajaykumar, C.R. Deepak and K.V.V. Aditya, Weldability, Machinability and Surfacing of Commercial Duplex Stainless Steel AISI2205 for Marine Applications—A Recent Review, *J. Adv. Res.*, 2017, **8**(3), p 183–199
20. Z.H. Rao, S.M. Liao and H.L. Tsai, Effects of Shielding Gas Compositions on Arc Plasma and Metal Transfer in Gas Metal Arc Welding, *J. Appl. Phys.*, 2010, **107**(4), p 044902
21. J. Norrish, *Advanced Welding Processes*, Elsevier, Amsterdam, 2006
22. F. Hejripour, F. Binesh, M. Hebel and D.K. Aidun, Thermal Modeling and Characterization of Wire Arc Additive Manufactured Duplex Stainless Steel, *J. Mater. Process. Technol.*, 2019, **272**, p 58–71
23. G.R. Mohammed, M. Ishak, S.N. Aqida and H.A. Abdulhadi, Effects of Heat Input on Microstructure, Corrosion and Mechanical Characteristics of Welded Austenitic and Duplex Stainless Steels: A Review, *Metals*, 2017, **7**(2), p 39
24. J. Nowacki and A. Lukojc, Structure and Properties of the Heat-Affected Zone of Duplex Steels Welded Joints, *J. Mater. Process. Technol.*, 2005, **164**, p 1074–1081
25. E.G. Betini, F.C. Cione, C.S. Mucsi, M.A. Colosio, J.L. Rossi, and M.T.D. Orlando, Experimental Study of the Temperature Distribution in Welded Thin Plates of Duplex Stainless Steel for Automotive Exhaust Systems, *SAE 2016 World Congress and Exhibition*, 2016, 2016-01-0503
26. V.A. Hosseini, L. Karlsson, D. Engelberg and S. Wessman, Time-Temperature-Precipitation and Property Diagrams for Super Duplex Stainless Steel Weld Metals, *Weld. World*, 2018, **62**(3), p 517–533
27. L. Karlsson, Intermetallic Phase Precipitation in Duplex Stainless Steels and Weld Metals Metallurgy, Influence on Properties and Welding Aspects, *Weld. World*, 1999, **43**(5), p 20–41
28. M.A. Valiente Bermejo, K. Hurtig, D. Eyzop and L. Karlsson, A New Approach to Study of Multi-pass Welds Microstructure and Properties of Welded 20-Mm-Thick Super Duplex Stainless Steel, *Appl. Sci.*, 2019, **9**(6), p 1050
29. D. Arun, K.D. Ramkumar and R. Vimala, Multi-Pass Arc Welding Techniques of 12 mm Thick Super-Duplex Stainless Steel, *J. Mater. Process. Technol.*, 2019, **271**, p 126–143
30. J. Verma and R.V. Taiwade, Effect of Welding Processes and Conditions on the Microstructure, Mechanical Properties and Corro-

- sion Resistance of Duplex Stainless Steel Weldments—A Review, *J. Manuf. Process.*, 2017, **25**, p 134–152
31. B. Lee, H. Lee and Y. Shin, Intergranular Corrosion Characteristics of Duplex Stainless Steel at Various Interpass Temperatures, *Int. J. Electrochem. Sci.*, 2015, **10**, p 7535–7547
 32. EN ISO 6947, Welding and Allied Processes—Welding Positions, 2011
 33. K. Singh, V. Sahni and S. Pandey, Slag Recycling in Submerged Arc Welding and Its Influence on Chemistry of Weld Metal, *Asian J. Chem.*, 2009, **21**(10), p 47–51
 34. S. Rhee and E. Kannatey-Asibu Jr., Observation of Metal Transfer during Gas Metal Arc Welding, *Weld. J.*, 1992, **71**, p 381
 35. S. Lu, H. Fujii and K. Nogi, Marangoni Convection and Weld Shape Variations in Ar–O₂ and Ar–CO₂ Shielded GTA Welding, *Mater. Sci. Eng. A*, 2004, **380**(1–2), p 290–297
 36. X. Xu, J. Ding, S. Ganguly, C. Diao and S. Williams, Preliminary Investigation of Building Strategies of Maraging Steel Bulk Material Using Wire + Arc Additive Manufacture, *J. Mater. Eng. Perform.*, 2019, **28**(2), p 594–600
 37. E. Brandl, A. Schoberth and C. Leyens, Morphology, Microstructure, and Hardness of Titanium (Ti-6Al-4V) Blocks Deposited by Wire-Feed Additive Layer Manufacturing (ALM), *Mater. Sci. Eng. A*, 2012, **532**(3), p 295–307
 38. G.P. Dinda, A.K. Dasgupta and J. Mazumder, Laser Aided Direct Metal Deposition of Inconel 625 Superalloy: Microstructural Evolution and Thermal Stability, *Mater. Sci. Eng. A*, 2009, **509**(1), p 98–104
 39. X. Xing, G. Qin, Y. Zhou, H. Yu, L. Liu, L. Zhang and Q. Yang, Microstructure Optimization and Cracking Control of Additive Manufactured Bainite Steel by Gas Metal Arc Welding Technology, *J. Mater. Eng. Perform.*, 2019, **28**(8), p 5138–5145
 40. H. Sieurin, *Fracture Toughness Properties of Duplex Stainless Steels*, Royal Institute of Technology, Stockholm, 2006
 41. V. Muthupandi, P.B. Srinivasan, S.K. Seshadri and S. Sundaresan, Effect of Weld Metal Chemistry and Heat Input on the Structure and Properties of Duplex Stainless Steel Welds, *Mater. Sci. Eng. A Struct.*, 2003, **358**, p 9–16
 42. Aircraft Materials, *Stainless Steel ER2209 Technical Data Sheet*, 2018, <https://www.aircraftmaterials.com/data/weld/er2209.html>

Publisher's Note Springer Nature remains neutral with regard to jurisdictional claims in published maps and institutional affiliations.